OE Optical Engineering

RESEARCH PAPER

Performance benefits of charge-domain gain in active shortwave infrared targeting

Derek Burrell,[a,*] **Joshua Follansbee**,[a] **Orges Furxhi**,[a] **Mark Spencer**,[b] **John Lund**,[c] **C. Kyle Renshaw**,[d] **and Ronald Driggers**[a]

[a]The University of Arizona, Wyant College of Optical Sciences, Tucson, Arizona, United States
[b]Air Force Institute of Technology, Department of Engineering Physics, Dayton, Ohio, United States
[c]The University of Alabama in Huntsville, System Management and Production Center, Huntsville, Alabama, United States
[d]University of Central Florida, College of Optics and Photonics, Orlando, Florida, United States

ABSTRACT. The sensitivity of active targeting systems in the shortwave infrared band is currently limited by high read noise associated with conventional readout integrated circuitry. This limit imposes a barrier to leveraging other performance trades, such as source power, illumination wavelength, and temporal coherence. Introducing gain in the charge domain prior to signal readout can reduce the impact of read noise, to the point that it no longer limits performance. In preparation for a series of planned active-imaging field tests, we demonstrate improved system performance on a modeling basis with two different charge-domain gain cameras: the electron bombarded active pixel sensor (EBAPS) and the mercury cadmium telluride avalanche photodiode sensor. We find that both solutions mitigate read noise to make either one suitable for laser range gating, but the high dark current associated with EBAPS may make it unsuitable for continuous-wave imaging in some scenarios. These results aid in our understanding of expected performance in field testing of charge-domain gain systems.

Keywords: active imaging; electron multiplication; range gating; shortwave infrared

Paper 20230642G received Jul. 4, 2023; revised Dec. 10, 2023; accepted Jan. 3, 2024; published Jan. 31, 2024.

1 Introduction

Imaging in the shortwave infrared (SWIR) band (i.e., at wavelengths in the range ~1.1 to 1.7 μm) has distinct advantages over other reflective bands, including higher atmospheric transmission, reduced optical turbulence, superior haze penetration, enhanced target/background contrast, and improved spectral discrimination.[1,2] Additionally, SWIR permits seeing laser designators and leveraging airglow in otherwise low-light environments.[3,4] SWIR capabilities have also reached technological maturity due to minimal losses in fiber-optic telecommunications and uncooled operation of indium gallium arsenide (InGaAs) detectors.[5,6] For all its benefits, however, passive SWIR imaging can suffer from low signal-to-noise ratios (SNRs) under reduced illumination conditions (e.g., at night).[7] Providing an active illumination source can remedy this problem in exchange for added size, weight, power, and cost (SWaP-C).

Another known issue with imaging in the SWIR band is that commercial off-the-shelf (COTS) cameras are often severely read-noise limited (in the hundreds of electrons),[8] potentially masking any performance boost over imagers in other bands with lower read noise (also known

*Address all correspondence to Derek Burrell, derekburrell@optics.arizona.edu

as temporal dark noise[9]). Improved readout integrated circuit design is one possible path forward. Another is to exploit the photoelectric effect by one of several mechanisms that provide amplification in the charge domain (i.e., electron multiplication), prior to both voltage conversion and digitization (after which analog and digital gain may be applied, respectively). Electron multiplication generally allows for higher dynamic range than analog gain by employing multiplication registers with their own full-well capacities between the serial registers and output nodes, so as not to affect the imaging area's well depth.

One such gain architecture is the patented electron bombarded active pixel sensor (EBAPS) from EOTECH (formerly Intevac Photonics).[10–12] The principle of EBAPS operation is that a GaAs photocathode absorbs incoming photons, which then accelerate through high voltage to a CMOS anode, generating a photocurrent for amplification prior to readout. The drawback of this photoemissive scheme is that excess noise—i.e., multiplicative noise arising from uncertainty in the electron multiplying process—becomes significant due to electron scattering within the multiplication layer,[13] effectively acting as a shot-noise multiplier. Consequently, the high dark current associated with EBAPS is poorly suited to long exposures with sources operating in continuous-wave (CW) mode. A solution to this problem is to implement laser range gating (LRG) with a pulsed laser source, thereby minimizing integration time (on the order of nanoseconds) and preventing significant accumulation of dark shot noise. LRG has many benefits, including contrast improvements by decreasing the influence of laser backscatter and solar path radiance, as well as reduction in scene clutter by effectively isolating the target from the background.[14,15]

A mercury cadmium telluride avalanche photodiode (MCT-APD) sensor can offer comparable gain that is virtually free of excess noise (albeit at a substantially higher market price),[16,17] enabling CW-mode imaging as needed with minimal dark current. APDs operate in reverse bias just below the breakdown voltage, causing incident photons to excite electrons that generate secondary carriers in an avalanche process. The favorable sensitivity of this device (as compared to, say, an InGaAs-APD) follows from avalanche breakdown being initiated by only a single carrier (i.e., electron or hole injection) as a result of MCT's unique band structure and scattering behavior.[18,19] An example COTS product incorporating MCT-APD technology is First Light Imaging's C-RED One, which claims subelectron total dark noise (i.e., shot noise and read noise combined).[20]

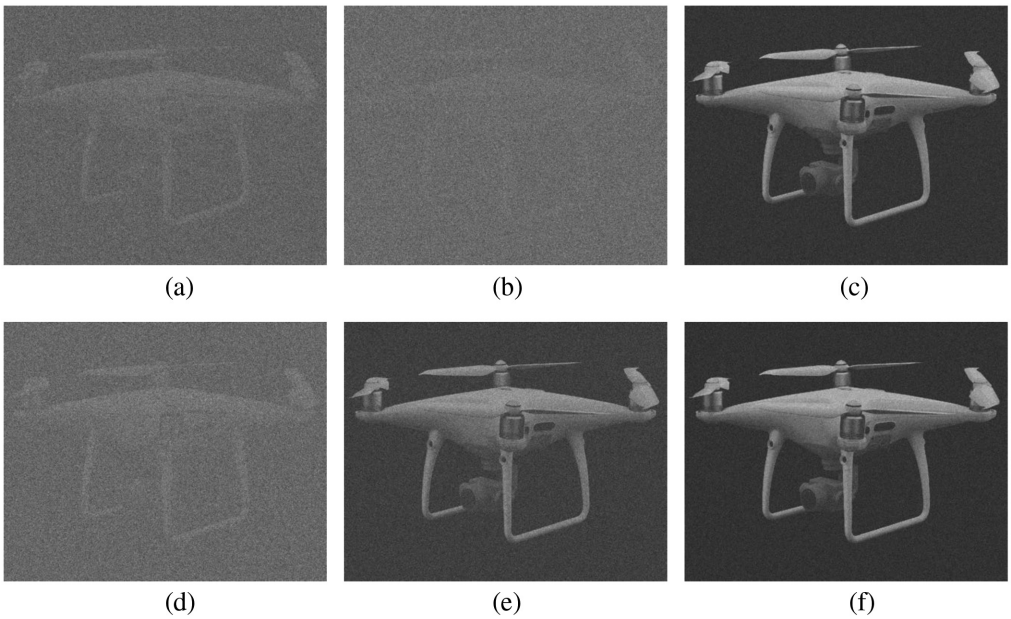

Fig. 1 Illustrative example of DJI Phantom 4 Pro V2.0 (CAD model) with simulated noise corresponding to (a) InGaAs, (b) EBAPS, and (c) MCT-APD detector specifications (c.f., Tables 1–3) in CW mode; same for (d)–(f) but in LRG mode. Target is taken to be at a range of 10 km through a clear atmosphere (without regard for resolution in this instance) and a peak integrated photon energy of 1225 (at 1.6 μm).[21]

Figure 1 uses pristine drone imagery with real noise parameters to illustrate the advantages of both gain cameras: In CW mode (top row), higher dark current counteracts the low read noise that EBAPS affords, making MCT-APD the preferred option; in LRG mode (bottom row), the two gain solutions would appear more or less indistinguishable from one another if their quantum efficiencies (QEs) were equal. Note that all noise throughout this paper is treated as temporal only; i.e., we assume no spatial noise in our modeling.

A third class of charge-domain amplification that includes photomultiplier tubes and image intensifier tubes is outside the scope of our present discussion, as these devices are generally restricted to ultraviolet, visible (VIS), and near-infrared radiation only. Given these considerations, we set out to compare performance of three SWIR imagers: a standard InGaAs (so-called "nongain"), an EBAPS, and an MCT-APD camera. In doing so, we outline a multifaceted tradespace with field-testing applicability in mind: 2 imaging geometries (ground to air [G2A], air to air [A2A]) × 3 target objects (white quadcopter drone, steel cylinder, and aluminum sheet) × 2 meteorological conditions (23-km visibility and 5-km visibility) × 2 illumination modes (CW and LRG) × 3 ambient lighting scenarios (day w/sun behind sensor [SBS], day w/sun behind target [SBT], night) = 72 excursions with each camera. Our goal in this performance comparison is to set expectations for a series of upcoming field tests designed to gauge image quality at 1.6 μm with an emphasis on active tracking. The coming sections tell this story by first discussing theory and inputs to our model, then detailing hardware parameters of a notional active testbed, and finally presenting results of our trade studies from which we can draw conclusions going forward.

2 Theory and Modeling

2.1 Sensitivity and Resolution

The metric of interest for sensitivity is generally an SNR or contrast-to-noise ratio (CNR), depending on the imaging task at hand. We have observed in preliminary tracking studies that aimpoint maintenance is more of a target detection problem than recognition or identification,[22] and so CNR is more pertinent to our interests. A general definition for this quantity is[23]

$$\mathrm{CNR} = \frac{\sqrt{(\mu_{\mathrm{tg}} - \mu_{\mathrm{bg}})^2 + \sigma_{\mathrm{tg}}^2}}{\sqrt{(F\sigma_{\mathrm{ps}})^2 + (F\sigma_{\mathrm{ds}})^2 + (\sigma_{\mathrm{rd}}/G)^2}}, \tag{1}$$

where μ_{tg}, μ_{bg}, σ_{tg}, σ_{ps}, σ_{ds}, and σ_{rd} are, respectively, the target signal mean, background signal mean, target signal variation, photon shot noise, dark shot noise, and read noise. The notation of Eq. (1) assumes all terms expressed in the charge domain (e^-), where the latter three refer specifically to background noise. Because shot noise is modeled as a Poisson process of equal mean and variance, $\sigma_{\mathrm{ps}} = \sqrt{\mu_{\mathrm{bg}}}$ and $\sigma_{\mathrm{ds}} = \sqrt{i_{\mathrm{d}}t}$ with i_{d} and t being the per-pixel dark current ($\mathrm{e}^-/\mathrm{px}/\mathrm{s}$) and integration time (s), respectively. F and G in Eq. (1) are, respectively, the excess noise factor and electron-multiplying gain of such devices as EBAPS and MCT-APD; as a reference, $F \approx \sqrt{2}$ for electron-multiplying charge-coupled devices.[23] We rely primarily on the Night Vision Integrated Performance Model (NV-IPM) to evaluate each of these terms,[24,25] though we have also developed our own radiometric model in Python for further verification with generally strong agreement.[26] Note that the denominator of Eq. (1) takes the form of a quadrature sum due to the uncorrelated nature of individual noise contributions. Also note that we are neglecting sources of coherent noise (e.g., speckle and scintillation) in this work as they affect only noise across the target and not the background.

We assess limiting image resolution simply in terms of nominal pixels on target (POT), estimated as[27]

$$\mathrm{POT} = \left(\frac{W/R}{d/f}\right)^2 \tag{2}$$

in the case of sampling-limited imagery.[28] Here W is the target's characteristic dimension (i.e., the square root of its surface area), R is the range from target to entrance pupil, d is the pixel pitch/width, and f is the effective focal length. Under the paraxial approximation, the numerator

and denominator of Eq. (2) are the target's angular extent and the camera's instantaneous field of view (IFOV), respectively.

Empirical evidence from tracking simulations has repeatedly suggested that a minimum CNR of 10 and POT of 50 are sufficient to consistently track without risking a breaklock event.[22] As such, we define a pass/fail figure of merit (FOM) as

$$\mathrm{FOM}(\mathrm{CNR}, \mathrm{POT}) = \mathrm{step}(\mathrm{CNR} - 10) \times \mathrm{step}(\mathrm{POT} - 50), \tag{3}$$

where[29]

$$\mathrm{step}(w) = \begin{cases} 1, & w > 0 \\ 1/2, & w = 0 \\ 0, & w < 0 \end{cases} \tag{4}$$

is the Heaviside step function and FOM > 0 to maintain a successful track. Figure 2 provides a visual for this FOM with darker shading indicative of acceptable CNR and POT.

2.2 NV-IPM Modifications

NV-IPM has a rich history of use in the passive electro-optical/infrared targeting community, and it is rigorously parameterized as such to predict targeting task performance.[30] We refer the interested reader to Teaney and Reynolds[24] for a broad overview of native NV-IPM interfacing, noting that all noise sources are modeled in NV-IPM as zero-mean Gaussian processes. Some retrofitting via custom components[31] is required to apply the model in cases of active imaging, however. For instance, NV-IPM does not natively account for laser backscatter through an aerosol volume. To implement this missing functionality, we assume a layered atmospheric model by dividing the space between target and sensor into M layers of equal thickness Δr (km). With a known aerosol phase function $f_{\mathrm{p}}(\theta_{\mathrm{i}}, \theta_{\mathrm{s}})$ that factors in respective incident and backscattered angles θ_{i} and θ_{s}, the backscattered path radiance from layer m is then

$$L_m = E_m \cdot N\sigma f_{\mathrm{p}}(0,0)\Delta r. \tag{5}$$

In the above, E_m is the irradiance at layer m, N is the aerosol number density, and σ is the scattering cross section, and the 0-deg arguments denote normal incidence and on-axis observation. In turn, transmittance ($0 \leq \tau \leq 1$) through the m'th layer is

$$\tau_m = \tau_{1\mathrm{k}}^{m\Delta r}, \tag{6}$$

where $\tau_{1\mathrm{k}}$ is a reference transmittance derived from the MODTRAN radiative-transfer code[32] for a 1-km path that accurately portrays the imaging geometry.

We estimate the unknowns in Eq. (5) from a literature review of Mie scattering theory, which describes particles on the order of an optical wavelength.[33,34] Elterman found in his own literature review that the Mie scattering coefficient ($\beta_{\mathrm{M}} = N\sigma$) decreases monotonically with

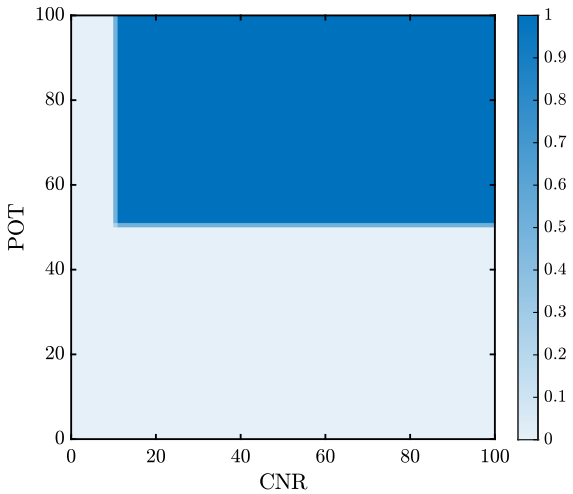

Fig. 2 Heatmap of pass/fail FOM as a function of both CNR and POT.

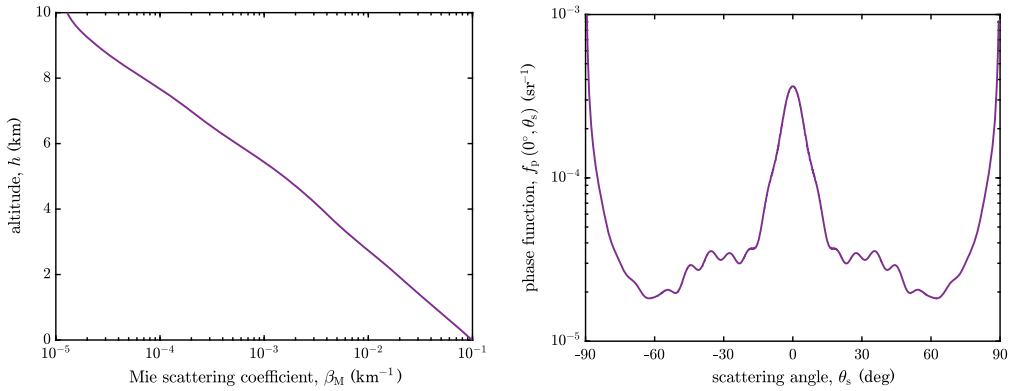

Fig. 3 (a) Mie scattering coefficient as a function of altitude. (b) Aerosol phase function at normal incidence as a function of scattering angle.

increasing wavelength, as does the aerosol number density with increasing altitude h (at least within the first 10 km above sea level).[35] Based on these findings, together with[36]

$$\beta_M(h) = \beta_M(0) \cdot \frac{N(h)}{N(0)}, \tag{7}$$

we plot the Mie scattering coefficient as a function of altitude in Fig. 3(a). At sea level and wavelength $\lambda = 1.6$ μm, this gives us $\beta_M(0) \approx 9.89 \times 10^{-2}$ km^{-1}. We then use the built-in Mie model of FRED Optical Engineering Software to derive the normally incident phase function of Fig. 3(b) from a uniform particle-size distribution between 0.001 and 10 μm[37] with a water refractive index of $n = 1.32$ at $\lambda = 1.6$ μm.[38] This leads to an on-axis value of $f_p(0,0) \approx 3.64 \times 10^{-4}$ sr^{-1}, along with an unnormalized phase function of $\beta_M(0) f_p(0,0) \approx 3.60 \times 10^{-8}$ (m · sr)$^{-1}$ that is consistent with the peer-reviewed literature.[39]

NV-IPM also lacks native capability to include solar path radiance between the target and sensor, which we must include in daytime engagements where active and passive signals combine at the receiver. We accomplish this by applying the expression

$$L(r) = L_{1k} \cdot \frac{1 - \tau(r)}{1 - \tau_{1k}}, \tag{8}$$

where L_{1k} is a 1-km reference path radiance output from MODTRAN, $\tau(r)$ is a range-dependent transmittance output from MODTRAN, and τ_{1k} is the reference transmittance we defined previously in Eq. (6).

3 Hardware Parameters

With a modeling approach in place, we now tailor our parameter space to hardware specifications for our notional testbed. Table 1 lists all parameters that are common to different excursions. For our pulsed system, we choose a somewhat arbitrary but realistic pulse energy of 200 mJ with a duration of 4 ns at a 10-Hz repetition rate. This translates to 2 W of optical power in a CW system producing an equivalent number of photons per frame interval. 2.2-mrad laser divergence corresponds to a Thorlabs F230SMA-1550 fiber collimator, and we assume the 50-nm bandwidth of an Edmund Optics #87-872 bandpass filter to suppress unwanted ambient light. We select an $f/4$ optical system based on COTS telescope availability with an acceptable balance between SWaP-C, FOV, and throughput.

We base our notional detector model on the specifications of an Allied Vision Goldeye CL-033 TEC1,[40] prominently featured in a number of active and passive SWIR systems. For our purposes, this means holding pixel size/pitch constant while varying noise parameters between camera models, in order to make a fair comparison between core technologies rather than discuss design differences. In particular, we assume the Goldeye's 5-μm pixel size/pitch.

Table 1 Source and sensor parameters that remain constant across excursions.

Parameter	Value
Laser wavelength, λ (μm)	1.6
Laser divergence, θ (mrad)	2.2
CW laser power, P_{CW} (W)	2
LRG pulse energy, Q_{LRG} (mJ)	200
LRG pulse duration, T_{LRG} (ns)	4
LRG repetition rate, ν_{LRG} (Hz)	10
Filter bandwidth, $\Delta\lambda$ (nm)	50
Aperture diameter, D (mm)	100
Focal length, f (mm)	400
Pixel size/pitch, d (μm)	5
Frame rate, ν_f (Hz)	10
CW integration time, Δt_{CW} (ms)	100
LRG integration time, Δt_{LRG} (ns)	100

Naturally, smaller pixels would have a beneficial effect on dark current, but our interest is in studying true noise specifications of commercially available devices. On the other hand, modeling actual differences in pixel size would expose somewhat trivial performance trades attributed to system resolution. Thus our hybrid approach offers a reasonable compromise to isolate noise performance through modeling. Table 2 summarizes all relevant noise parameters, with notable differences including a sharp decrease in read noise for both gain cameras but a drastic increase in dark current with EBAPS. The EBAPS system also has the lowest QE of the three, as shown in Fig. 4. The QE from each of these curves at $\lambda = 1.6$ μm makes up the third column of Table 2.

Table 3 shows the defining traits for our three targets of interest in order of increasing size (by area), and Fig. 5(a) provides a visualization of these target objects acquired for future testing. Using these dimensions in conjunction with the parameters in Table 1, we plot POT as a function of range for all three targets in Fig. 5(b). $F\lambda/d$ (where $F = f/D$ is the f-stop or focal ratio) according to Table 1 is 1.28, placing our system in the broad transition region between being sampling and diffraction limited.[41,42] It is, therefore, possible that our targets will become unresolved by the optics well before sampling, but we consider nominal pixel projections for the POT $\geq$ 50 criterion since object sizes on this order of magnitude are well resolved in our system by both definitions. To provide a reference value for extreme ranges at which CNR is of no consequence, we take the simplified approach of calling a target "unresolved" when it reaches POT = 1.

Table 2 Dark current, read noise, and QE values (at 1.6 μm) of all three camera systems under test.

Detector	Dark current, i_d (ke$^-$/px/s)	Read noise, σ_{rd} (e$^-$)	QE, η (%)
InGaAs	110	390	73.9
EBAPS	1400	1	25.1
MCT-APD	0.08	1	77.5

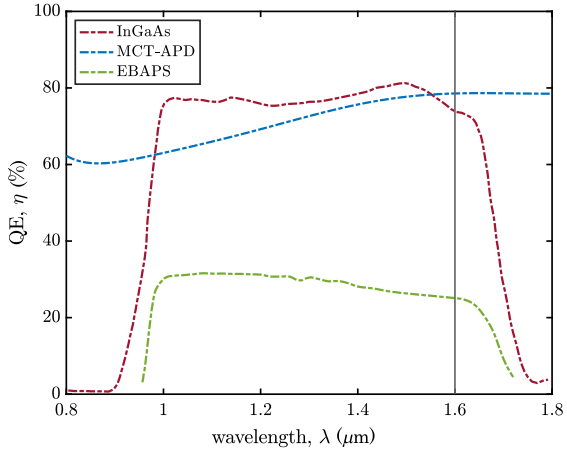

Fig. 4 QE of various cameras in the SWIR band per manufacturer datasheets.

Table 3 Characteristic dimensions and reflectivity values (at 1.6 μm) of all three target objects under test; obtained from material characterization of real objects.

Target object	Characteristic dimension, W (cm)	Reflectivity, ρ (%)
Quadcopter drone	10	74
Steel cylinder	29	70
Aluminum sheet	47	97

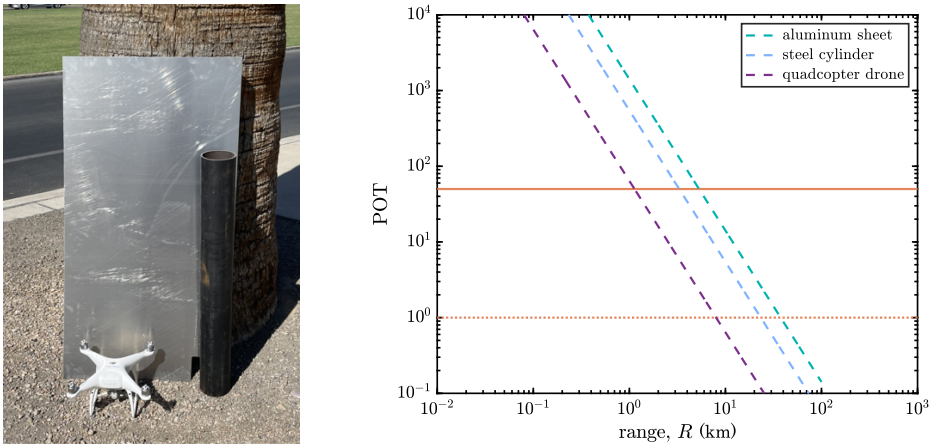

(a) (b)

Fig. 5 (a) Photograph of target objects planned for use in upcoming field tests. (b) POT with respect to sampling as a function of range to various targets; solid and dotted orange lines represent POT = 50 and "unresolved" range (at which POT = 1), respectively.

4 NV-IPM Results and Discussion

For reference throughout this section, Fig. 6 shows the relative placement of Sun, sensor, and target in both SBS and SBT scenarios. Note that, for modeling purposes, the only passive signal is ambient sunlight diffusely scattered through clouds (modeled as a sum of transmitted and path radiances). Under the assumption that background pixels see ground projections of the IFOV, the irradiance on such pixels is therefore independent of range.

Looking closely at one subset of excursions, Fig. 7 displays all CNR versus range results in the case of an aluminum sheet in a G2A imaging geometry. Specifically, its first, second, and

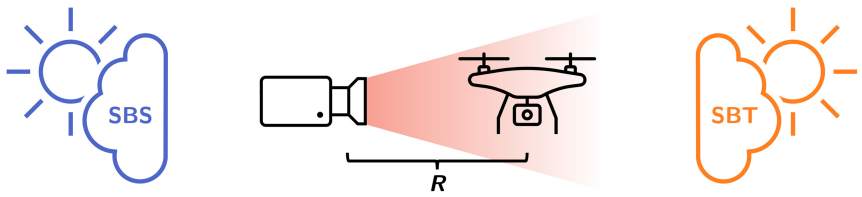

Fig. 6 Diagram illustrating toy model of active imaging at range R in SBS and SBT scenarios.

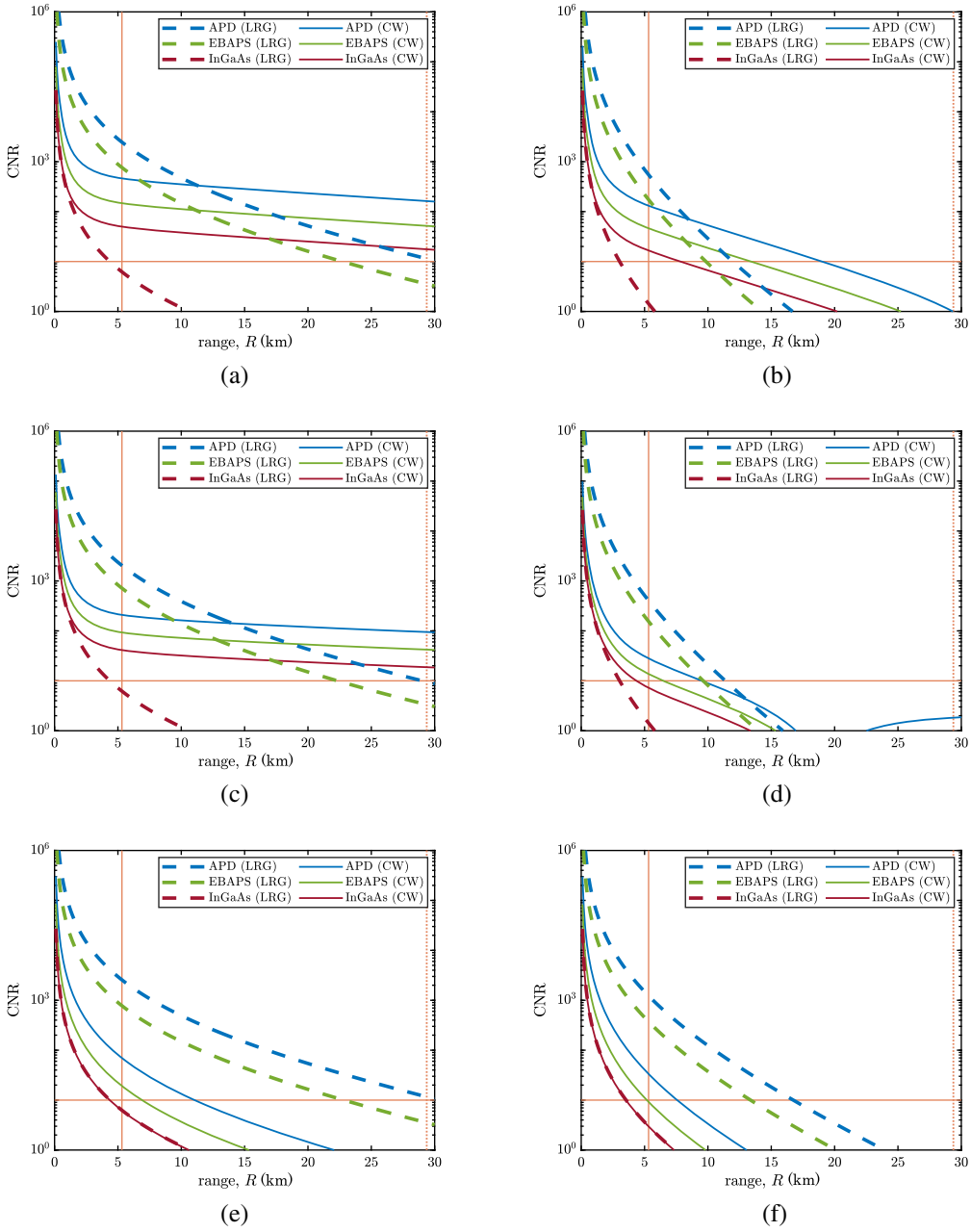

Fig. 7 CNR as a function of range for G2A imaging of an aluminum sheet; orange lines represent CNR = 10 (solid horizontal), POT = 50 (solid vertical) and "unresolved" range (dotted vertical). (a) Daytime SBS 23-km visibility, (b) daytime SBS 5-km visibility, (c) daytime SBT 23-km visibility, (d) daytime SBT 5-km visibility, (e) nighttime 23-km visibility, and (f) nighttime 5-km visibility.

third rows comprise a daytime SBS scenario, a daytime SBT scenario, and a nighttime scenario, respectively; its left and right columns, respectively, represent 23-km and 5-km visibility conditions.

The general shape comparison between LRG and CW curves is quite intuitive, as the pulsed laser provides a stronger signal at close range that falls off with distance as an inverse-square law. Passive illumination, on the other hand, maintains virtually constant irradiance with target distance. For this reason, long-range applications may benefit from CW mode in the presence of ambient lighting with little benefit from a divergent laser source. InGaAs operating in the read-noise limit experiences none of the usual LRG advantages, with performance either suffering compared to CW during daytime or matching CW at nighttime.

Performance in CW mode generally degrades with successive rows, as path radiance is most severe with SBT and the only available signal is subject to strong laser backscatter at nighttime. Columnwise, CNR suffers more in 5-km than 23-km visibility across the board. The degradation from SBS to SBT is less dramatic for LRG, however, and nighttime LRG imaging is superior due to a strong signal with minimal backscatter and zero contribution from solar path radiance. Beyond our binary FOM > 0 test, it is noteworthy that the order of best to worst performance always goes from MCT-APD to EBAPS to InGaAs, with the difference between gain imagers owing to a combination of increased dark current and decreased QE in EBAPS. Also worth noting is that the CW-illuminated target and sky background undergo contrast reversals in Fig. 7(d) that give rise to local minima at longer ranges. Such reversals simply result from viewing targets of range-dependent brightness against a background of constant brightness: Its brightness exceeds that of the background at close ranges but eventually becomes dimmer than the background with increasing range.

In the interest of visualizing data over a wider array of cases, Fig. 8 compares maximum ranges at which CNR ≥ 10 for both G2A [(a) and (b)] and A2A [(c) and (d)] geometries with the

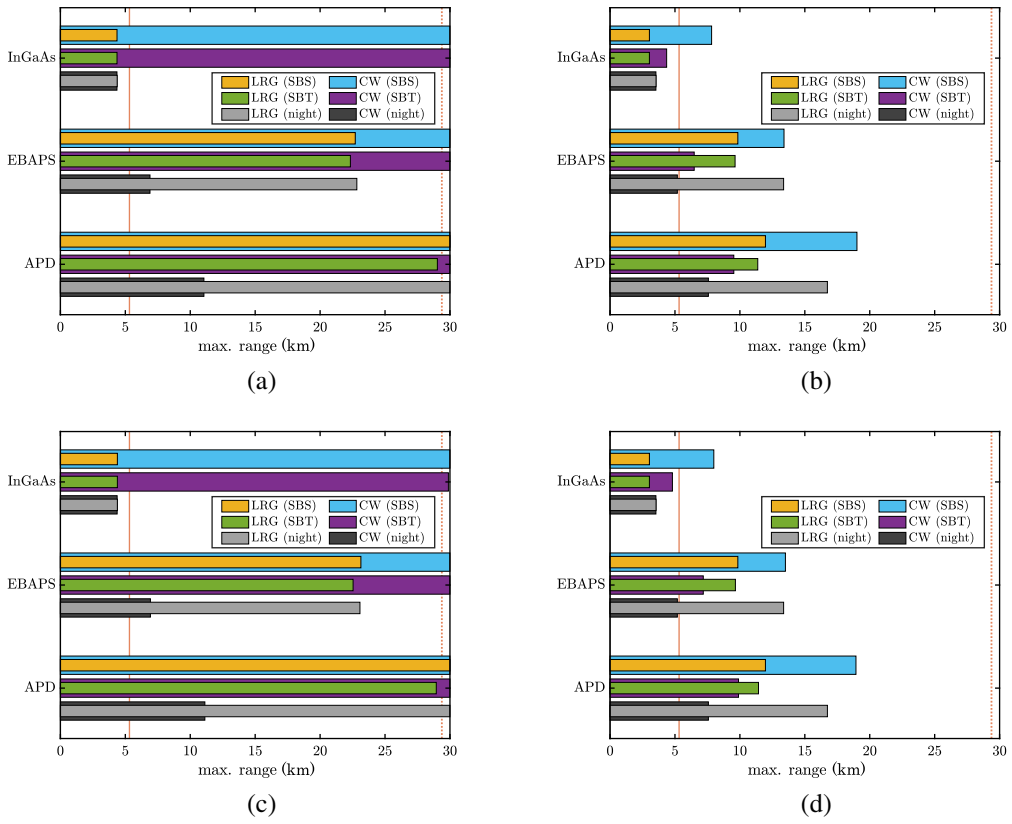

Fig. 8 Comparison between maximum ranges for an aluminum sheet; orange vertical lines represent POT = 50 (solid) and "unresolved" range (dotted). (a) G2A 23-km visibility (b) G2A 5-km visibility, (c) A2A 23-km visibility, and (d) A2A 5-km visibility.

target again being an aluminum sheet. The columns once again represent 23-km and 5-km visibility from left to right. In a clear atmosphere with 23-km visibility, daytime CNR remains above 10 well past the "unresolved" range for any system operating in CW mode. When paired with a gain camera, CW illumination is more than sufficient for CNR ≥ 10 to surpass the POT ≥ 50 cutoff in all daytime scenarios. The reason for CW outperforming LRG in daylight is that CNR benefits more from longer integration of ambient sunlight than it suffers from increased path radiance and dark current. When nighttime imaging is also a priority, however, one of the gain systems operating in LRG mode is generally necessary to reach the POT limit. Again we can see here that CW and LRG perform identically in all nighttime cases with an InGaAs camera as limited by read noise. The MCT-APD either outperforms or is tied with other systems in all cases, as it has no inherent drawback other than price. EBAPS would perform similar to MCT-APD in all LRG cases (where dark current is negligible) if not for its comparatively low QE. Overall, LRG performance of a given camera stays relatively constant in different lighting scenarios because gating reduces the impact of both ambient signal and path radiance.

For further abstraction of results, we plot maximum ranges, in which CNR ≥ 10 for each gain camera versus InGaAs across all 72 excursions in Fig. 9(a). We immediately notice that gain cameras outperform nongain as expected, but distances from the diagonal provide a sense of relative performance distribution (keeping in mind that points overlap in some instances). Rather than consider maximum range, Fig. 9(b) compares CNR values for each gain camera versus InGaAs at the ranges where POT $= 50$. Here we see a clear divide between high and low visibility, as well as division between gain cameras within each of these regimes. Together these two plots illustrate that MCT-APD will deliver better results than EBAPS or InGaAs when considering either CNR ≥ 10 or POT ≥ 50 alone, but EBAPS performance is likely acceptable when considering both criteria together (especially with LRG rather than CW illumination).

The nighttime-only results of Fig. 10 show the same trends, with fewer cases out at longer ranges but a similar distribution of cases otherwise. The main takeaway from Figs. 9 and 10 is that EBAPS can be a lower-cost alternative to MCT-APD and still a marked improvement over InGaAs for an LRG system to achieve FOM > 0, but MCT-APD is the best all-purpose camera that may justify its cost if nighttime CW imaging at long range is a must. It is also important to note, however, that COTS detector arrays are currently limited to larger pixel sizes/pitches with MCT-APD (~25 μm) than with EBAPS (~15 μm). Since we have studied only G2A and A2A imaging with nominally zero background reflectivity up to this point, we can expect that LRG would compare even more favorably to CW in G2G or A2G geometries with a substantial

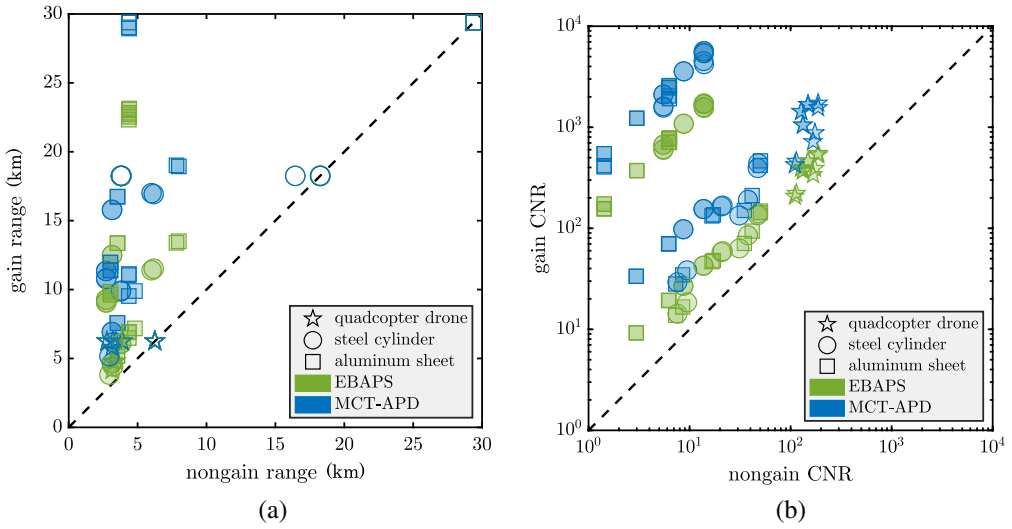

Fig. 9 (a), (b) Summary of gain versus nongain relative performance for all excursions within tradespace; unfilled markers in (a) indicate CNR ≥ 10 beyond "unresolved" range. Diagonal reference line marks equivalent performance and thus no improvement.

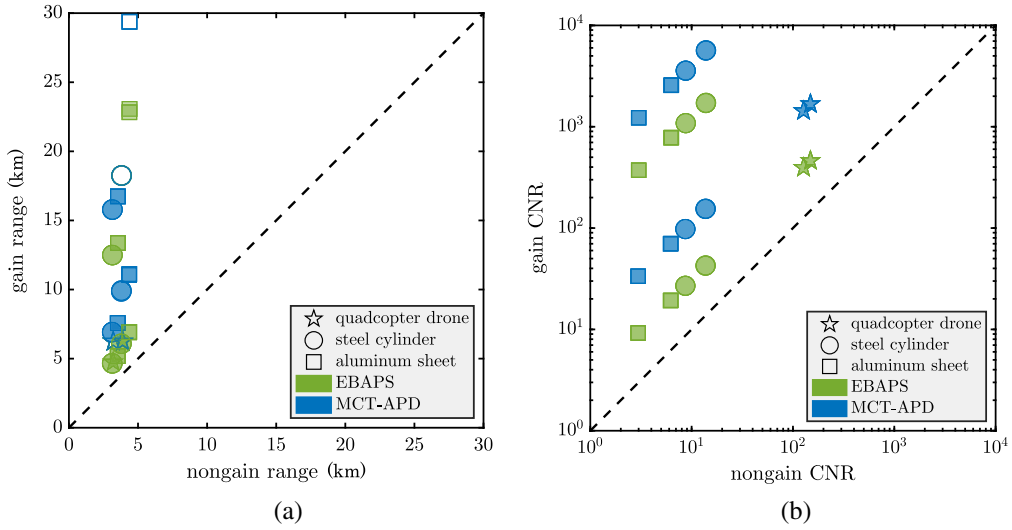

Fig. 10 (a), (b) Summary of gain versus nongain relative performance for "nighttime-only" excursions within tradespace; unfilled shapes in (a) indicate CNR ≥ 10 beyond "unresolved" range. Diagonal reference line marks equivalent performance and thus no improvement.

background to isolate from the target. The same is true of harsher environments, such as haze, rain, or smoke, where one could expect backscatter to limit performance even more severely than in cases we have explored here.

5 Conclusion

The sensitivity of active targeting systems in the SWIR band is currently limited by high read noise associated with conventional readout integrated circuitry. This limit imposes a barrier to leveraging other performance trades, such as source power, illumination wavelength, and temporal coherence. Introducing gain in the charge domain prior to signal readout can reduce the impact of read noise, to the point that it no longer limits performance. In preparation for a series of planned active-imaging field tests, we demonstrated improved system performance on a modeling basis with two different charge-domain gain cameras: the EBAPS and the MCT-APD sensor. We found that both solutions mitigate read noise to make either one suitable for LRG, but the high dark current associated with EBAPS may make it unsuitable for CW imaging in some scenarios. These results aid in our understanding of expected performance in field testing of charge-domain gain systems.

Disclosures

This paper was previously accepted as Paper 12533-12 for presentation in Defense + Commercial Sensing 2023. It was ultimately withdrawn from the proceedings because of delays in obtaining approval for public release. This paper is now approved for public release: distribution is unlimited.

Code and Data Availability

Raw data that support the findings of this article are not publicly available at this time. They can be requested from the corresponding author upon reasonable request.

Acknowledgments

This material is based upon work supported by the Army Contracting Command-Aberdeen Proving Ground (ACC-APG), Adelphi Contracting Division (Contract No. W911QX22C0034). Any opinions, findings, and conclusions or recommendations expressed in this material are those of the authors and do not necessarily reflect the views of the ACC-APG, Adelphi Contracting Division.

References

1. R. G. Driggers, V. Hodgkin, and R. Vollmerhausen, "What good is SWIR? Passive day comparison of VIS, NIR, and SWIR," *Proc. SPIE* **8706**, 87060L (2013).
2. "Short wave infrared (SWIR) for surveillance applications in defense," White Paper, Allied Scientific Pro, Gatineau, 2016, https://www.alliedscientificpro.com/blog/welcome-to-our-blogs-1/white-paper-short-wave-infrared-swir-for-surveillance-applications-in-defense-137.
3. M. L. Vatsia, U. K. Stich, and D. Dunlap, "*Night-sky radiant sterance from 450 to 2000 nanometers*," Tech. Rep. ECOM-7022, U.S. Army Electronics Command, Fort Monmouth (1972).
4. R. H. Vollmerhausen, R. G. Driggers, and V. A. Hodgkin, "Night illumination in the near- and short-wave infrared spectral bands and the potential for silicon and indium-gallium-arsenide imagers to perform night targeting," *Opt. Eng.* **52**(4), 043202 (2013).
5. J. P. Vermeiren and P. Merken, "InGaAs detectors and FPA's for a large span of applications: design and material considerations," *Proc. SPIE* **10563**, 1056313 (2017).
6. "A short introduction to shortwave infrared (SWIR) imaging," White Paper, Smart Vision Lights, Norton Shores, 2019, https://smartvisionlights.com/wp-content/uploads/SVL_SWIR-White-Paper.pdf.
7. A. Jones et al., "An advanced scattered moonlight model for Cerro Paranal," *Astron. Astrophys.* **560**, A91 (2013).
8. J. S. Dam, P. Tidemand-Lichtenberg, and C. Pedersen, "Continuous-wave near-photon counting spectral imaging detector in the mid-infrared by upconversion," *Proc. SPIE* **8726**, 87260X (2013).
9. "EMVA 1288 overview: Imaging performance," White Paper, Teledyne FLIR, Wilsonville. https://www.flir.com/discover/iis/machine-vision/emva-1288-overview-imaging-performance/.
10. V. W. Aebi and J. J. Boyle, "Electron bombarded active pixel sensor," Patent No. US6285018B1, EOTECH, LLC, Santa Clara (2001).
11. "Intevac's core sensor technology," White Paper, Intevac Photonics, Santa Clara, 2012, https://www.intevac.com/intevacphotonics/military/ebaps-technology-overview/.
12. EOTECH, LLC, Plymouth, "LIVAR®M506 gated SWIR camera system DS_1002.V1," 2022, https://www.eotechinc.com/media/documents/spec_sheets/2022_EOTECH_LIVAR_M506.pdf.
13. J. Bai et al., "The analysis of electron scattering among multiplying layer in EBAPS using optimized Monte Carlo method," *Mod. Phys. Lett. B* **34**(34), 2050398 (2020).
14. F. Christnacher et al., "Influence of gating and of the gate shape on the penetration capacity of range-gated active imaging in scattering environments," *Opt. Express* **23**, 32897–32908 (2015).
15. A. H. Willitsford et al., "Range-gated active short-wave infrared imaging for rain penetration," *Opt. Eng.* **60**(1), 013103 (2021).
16. M. A. Kinch et al., "HgCdTe electron avalanche photodiodes," *J. Electron. Mater.* **33**(6), 630–639 (2004).
17. "Answers to questions on MCT's advantages as an infrared imaging material," White Paper MR-2010-08-2_Rev02, Leonardo DRS, Electro-Optical & Infrared Systems, Dallas, 2010, https://www.leonardodrs.com/wp-content/uploads/2023/08/201306_advantages_of_mct.pdf.
18. J. Beck et al., "The HgCdTe electron avalanche photodiode," *J. Electron. Mater.* **35**(6), 1166–1173 (2006).
19. A. Singh, V. Srivastav, and R. Pal, "HgCdTe avalanche photodiodes: a review," *Opt. Laser Technol.* **43**(7), 1358–1370 (2011).
20. First Light Imaging, Meyreuil, "C-RED one product datasheet: ultra low noise ultra high speed SWIR camera," 2023, https://www.first-light-imaging.com/wp-content/uploads/2023/06/Datasheet_C-RED-One_01.06.2023.pdf.
21. J. Follansbee et al., "Radiometry and contrast-to-noise ratio for continuous-wave and laser range-gated active imaging systems," *Appl. Opt.* **62**, 9317–9325 (2023).
22. D. Burrell et al., "Testing for breaklock conditions of tracking algorithms," in *Annu. Directed Energy Sci. and Technol. Sympos.*, DEPS (2023).
23. M. S. Robbins and B. J. Hadwen, "The noise performance of electron multiplying charge-coupled devices," *IEEE Trans. Electron Devices* **50**(5), 1227–1232 (2003).
24. B. Teaney and J. Reynolds, "Next generation imager performance model," *Proc. SPIE* **7662**, 76620F (2010).
25. A. Irwin, "Performance prediction from EO system measurements using IRWindows and NV-IPM," *Proc. SPIE* **10625**, 1062502 (2018).
26. J. Follansbee et al., "Target acquisition performance comparison of active continuous-wave and range-gated imaging systems at 1.6 and 2.1 μm," *Opt. Eng.* **62**, 094107 (2023).
27. P. M. Moser, "Mathematical model of FLIR performance," Tech. Rep. NADC-20203:PMM, Naval Air Development Center, Warminster (1972).
28. B. P. Teaney and D. P. Haefner, "Evaluating the performance of an IR imaging system: a tutorial," *Proc. SPIE* **10625**, 106250K (2018).
29. J. D. Gaskill, *Linear Systems, Fourier Transforms, and Optics*, 1st ed., John Wiley & Sons, Hoboken (1978).

30. R. H. Vollmerhausen and E. Jacobs, "The targeting task performance (TTP) metric: a new model for predicting target acquisition performance," Tech. Rep. AMSEL-NV-TR-230, Modeling and Simulation Division, Night Vision and Electronic Sensors Directorate, U.S. Army CERDEC, Fort Belvoir (2004).
31. B. P. Teaney, D. P. Haefner, and S. D. Burks, "Custom component generation in the night vision integrated performance model," *Proc. SPIE* **9452**, 94520Q (2015).
32. A. Berk et al., *MODTRAN® 6.0 User's Manual*, Spectral Sciences, Inc., Burlington (2019).
33. S. Arridge et al., "Particle sizing in the Mie scattering region: singular-value analysis," *Inverse Probl.* **5**, 671–689 (1989).
34. M. Howard et al., "Mie scattering analysis: preliminary report," Tech. Rep. DOE/NV/25946–3086, Nevada National Security Site, Nye County (2016).
35. L. Elterman, "Parameters for attenuation in the atmospheric windows for fifteen wavelengths," *Appl. Opt.* **3**(6), 745–749 (1964).
36. R. G. Driggers, M. H. Friedman, and J. M. Nichols, *Introduction to Infrared and Electro-Optical Systems*, 2nd ed., Remote Sensing Library, Artech House, Norwood (2012).
37. J. Haywood, "Atmospheric aerosols and their role in climate change," Chapter 27 in *Climate Change*, T. M. Letcher, Ed., 2nd ed., pp. 449–463, Elsevier, Boston (2016).
38. G. M. Hale and M. R. Querry, "Optical constants of water in the 200-nm to 200-μm wavelength region," *Appl. Opt.* **12**(3), 555–563 (1973).
39. S. Chudamani, J. D. Spinhirne, and A. D. Clarke, "Lidar aerosol backscatter cross sections in the 2-μm near-infrared wavelength region," *Appl. Opt.* **35**(24), 4812–4819 (1996).
40. Allied Vision Technologies GmbH, Stadtroda, "Goldeye G/CL User Guide V4.6.2," 2022, https://cdn.alliedvision.com/fileadmin/content/documents/products/cameras/Goldeye_2/techman/Goldeye_G-CL_TechMan.pdf.
41. G. C. Holst and R. G. Driggers, "Small detectors in infrared system design," *Opt. Eng.* **51**(9), 096401 (2012).
42. J. Robinson et al., "Case for small pixels: system perspective and FPA challenge," *Proc. SPIE* **9100**, 91000I (2014).

Derek Burrell is a recent PhD graduate from the University of Arizona's Wyant College of Optical Sciences. He received his BS degree in electrical engineering from Michigan Technological University in 2018 and his MS degree in optics and photonics from the University of Central Florida in 2020. He has authored or coauthored 11 journal articles and 17 conference proceedings. His research focuses primarily on mitigating coherent effects in active electro-optical applications, specifically with respect to tracking and wavefront sensing. He is a member of SPIE.

Joshua Follansbee is a third-year PhD student at the University of Arizona's College of Optical Sciences. His work in the Professor Ronald Driggers' Group focuses on infrared imaging, particularly in actively illuminated systems.

Orges Furxhi holds his PhD in electrical engineering from the University of Memphis. He is a co-author in the third edition of the *Introduction to Infrared and Electro-optical System* book, has authored or co-authored more than 50 research publications, and has 5 issued patents.

Mark Spencer is the director of the Joint Directed Energy Transition Office within the Office of the Under Secretary of Defense for Research and Engineering. He is also an adjunct associate professor of optical sciences and engineering at the Air Force Institute of Technology within the Department of Engineering Physics. He is a fellow of SPIE.

John Lund is a principal research engineer at the University of Alabama Huntsville, assigned to the directed energy program office at the US Army Rapid Capability Critical Technology Office, focusing on new technology strategy and demonstration initiatives. He has almost four decades involvement in the production and modernization of military electro-optics systems. He majored in physics at Augustana College and holds two master of science degrees from Florida Institute of Technology.

C. Kyle Renshaw is an assistant professor in CREOL of the College of Optics and Photonics at the University of Central Florida, where he holds joint appointments in the Department of Physics and Electrical and Computer Engineering. He conducts research in materials, components, and technologies for imaging systems, including detector, focal plane, and lens technologies, along with system architectures. He is a member of the OSA, SPIE, and IEEE Photonics.

Ronald Driggers is a professor at Wyant College of Optical Sciences of the University of Arizona.